buildings

Article

Parametric Study on Seismic Performance of Slender T-Shaped RC Walls Subjected to Biaxial Loading

Mengzhen Wu [1,2,*], Bin Wang [1,2], Qingxuan Shi [1,2] and Wenzhe Cai [2,3]

[1] School of Civil Engineering, Xi'an University of Architecture & Technology, Xi'an 710055, China; wangbin@xauat.edu.cn (B.W.); shiqx@xauat.edu.cn (Q.S.)
[2] Key Lab of Structural Engineering and Earthquake Resistance, Ministry of Education, Xi'an University of Architecture & Technology, Xi'an 710055, China; caiwenzhe@xpu.edu.cn
[3] School of Urban Planning and Municipal Engineering, Xi'an Polytechnic University, Xi'an 710048, China
* Correspondence: wumengzhen@126.com

Abstract: To investigate the effects of parameters on the seismic performance of slender T-shaped RC walls subjected to a biaxial seismic action, a numerical model was established using a fiber-based cross-section and displacement-based beam–column element. The axial load ratio, shear span ratio, flange width to web height ratio, concrete strength grade, stirrup ratio, and longitudinal reinforcement ratio were selected for the parametric study, and the effects of these parameters on the performance degradation under biaxial loading were investigated. Furthermore, a sensitivity analysis of various parameters for the decrease was conducted. The results showed that the bearing and deformation capacities under biaxial loading were both decreased, and the total energy consumption was greater than that under uniaxial loading. The impacts of different parameters and loading paths on the decrease extent were significantly different, and the overall reduction was greater in the flange direction than in the web direction. Under the square loading path, the T-shaped wall had the greatest reduction in its seismic performance, followed by the eight-shaped and cruciform loading paths. The changes in the axial load ratio, shear span ratio, and concrete strength significantly affected the performance degradation under biaxial loading. Accordingly, it is recommended to reasonably consider the values of these three parameters in a multidimensional seismic design to maintain safety redundancy.

Keywords: T-shaped wall; biaxial loading; seismic performance; concrete structures; numerical analysis; performance degradation; structural analysis

Citation: Wu, M.; Wang, B.; Shi, Q.; Cai, W. Parametric Study on Seismic Performance of Slender T-Shaped RC Walls Subjected to Biaxial Loading. *Buildings* **2024**, *14*, 162. https://doi.org/10.3390/buildings14010162

Academic Editors: Francisco López-Almansa and Giuseppina Uva

Received: 12 October 2023
Revised: 4 January 2024
Accepted: 7 January 2024
Published: 9 January 2024

1. Introduction

Reinforced concrete (RC) walls possess great lateral resistance and are widely used as important seismic components in building structures [1–5]. The T-shaped wall is an integrated component composed of two orthogonal wall segments. The two segments will interact with each other in terms of damage, bearing capacity, and deformation capacity. Therefore, the stress characteristics of the T-shaped wall are significantly different from those of a regular rectangular wall [6]. Hence, it requires specific research on the structural performance of T-shaped walls. Currently, there is abundant research on T-shaped walls, including section design and optimization [7,8], shear capacity analysis [9], the use of high-strength reinforcement [10] or composites of steel and concrete [11], and so on.

Ground motion is usually multidimensional, and the response of structural components under a multidimensional ground motion excitation is significantly different from those under a uniaxial action [12]. The experimental research on seismic performance under biaxial loading mainly focuses on columns and RC walls with other cross-sectional shapes [13–16]. Due to the asymmetry of the cross section, there are differences in the mechanical performances of T-shaped walls in different directions. Furthermore, biaxial loading causes a biaxial coupling effect, which in turn affects the hysteresis performances of the T-shaped walls in two orthogonal directions. There is limited research on the seismic performance of slender T-shaped RC walls under biaxial loading [17–19]. Therefore, it is necessary to conduct a comprehensive study on the impact of different parameters on the biaxial coupling effect, and subsequently on the hysteresis performance of a T-shaped wall under biaxial loading.

Several studies have been conducted on the numerical analysis of T-shaped walls under biaxial loading [20–23], but most simulations use solid elements which require a large amount of computation. However, a parametric analysis under different biaxial loading paths requires a large number of models to be established, and using solid elements for the calculation requires a lot of time. OpenSees has adequate material constitutive properties and good nonlinear analysis capabilities, while using macroelement modeling. The model is simple, so it can balance efficiency and accuracy [24]. A few researchers have completed OpenSees modeling of biaxial-loaded T-shaped walls. Waugh [25] used a fiber-based analysis to model a four-story and a two-story T-shaped wall and simulated them under multiaxial loading. Kolozvari [26] developed a three-dimensional four-node element for the simulation of nonplanar RC walls under multidirectional loading, and calibrated and validated it against the experimental results of one T-shaped and one U-shaped RC wall. Wang [27] proposed a nonlinear model for flanged RC walls, considering the combined actions of bending and shear by using the stiffness-based fiber beam–column elements in OpenSees. The effects of influencing parameters on the seismic behavior of flanged RC walls were investigated. However, no further in-depth investigation has been conducted on the effects of different parameters in these studies.

In this study, the degradation of the seismic performance of T-shaped walls under biaxial loading was systematically analyzed. A numerical model of a slender T-shaped RC wall was established, and the mechanical behavior of the T-shaped wall under uniaxial and biaxial loadings was numerically simulated. The effects of six parameters and loading paths on the seismic performance degradation of the T-shaped wall under biaxial loading were studied. Finally, a sensitivity analysis of parameters for the degradation was conducted. This study can provide data support for subsequent research on the biaxial reduction factor.

2. Numerical Modeling of T-Shaped RC Walls under Biaxial Loading

2.1. Design Details of Experimental Specimens

Five slender T-shaped RC walls with identical dimensions and cross sections were experimentally studied by Wang [19]. The height of the wall was 2200 mm, and the dimensions of the flange and web segment were 900 mm $\times$ 100 mm. The design details of the specimen are shown in Figure 1, where the 6 mm bars are allowed to be used in seismic design according to the Chinese code for the design of concrete structures GB 50010-2010 [28]. The concrete strength grade was selected as C35, with the average compressive strength of 37.63 MPa. The reinforcement details were designed based on the Chinese standard JGJ-3 [29].

Since the experiment involved loading in two orthogonal directions, for the convenience of description, the loading direction and various parts of the T-shaped walls have been defined, as shown in Figure 2. The parts of the web and flange that were far from the intersection area were called the web tip and flange tip, respectively. The direction of loading to the web tip was specified as the positive direction of the web direction, and the direction of the first loaded flange tip was the positive direction of the flange direction.

Five T-shaped walls corresponded to five different loading paths, namely uniaxial loading along the web direction, uniaxial loading along the flange direction, biaxial loading under cruciform path, biaxial loading under square path, and biaxial loading under eight-shaped path, which are illustrated in Figure 3. The chosen axial load ratio was taken as 0.1. The horizontal biaxial loading adopted a displacement-controlled system throughout the entire test process. The specific loading procedure is described in study [18], and the applied displacements of biaxially-loaded specimens are plotted in Figure 4.

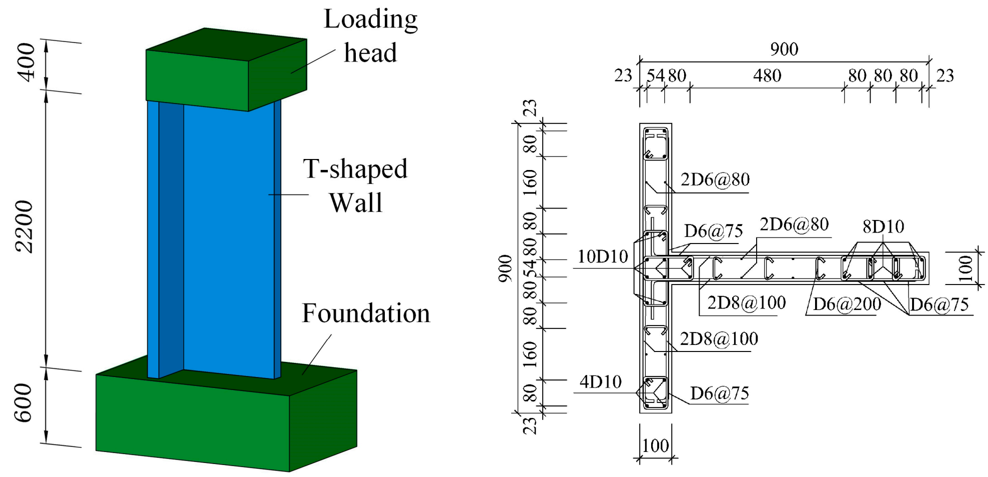

(**a**) (**b**)

Figure 1. Specimen details. (**a**) Elevation of specimen; (**b**) reinforcement details and section dimensions.

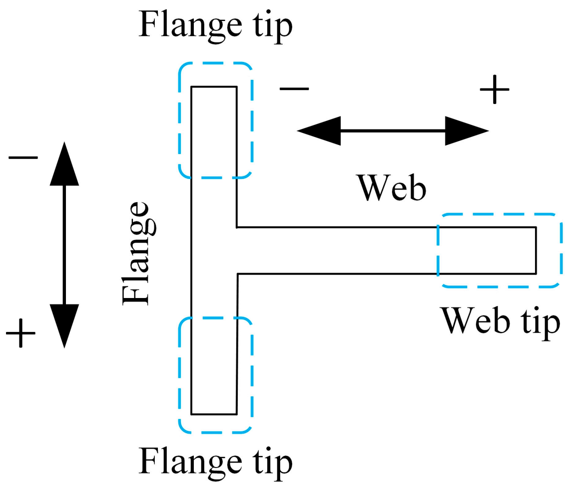

Figure 2. Loading direction.

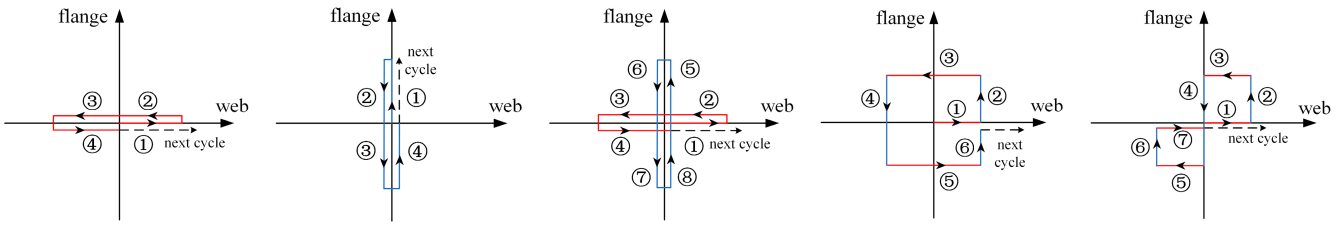

Figure 3. Loading paths. (**a**) Uniaxial loading along the web direction; (**b**) uniaxial loading along the flange direction; (**c**) cruciform loading path; (**d**) square loading path; (**e**) eight-shaped loading path.

All the specimens led to flexural failure because of the significant damage at the bottoms of web and flange tips. Horizontal cracks were first observed in the web tip, and these cracks gradually developed diagonally after the wall yielded. These diagonal cracks had a small width and were mainly concentrated in the lower parts of the wall. Biaxial loading paths did not change the failure pattern of the T-shaped wall, but only aggravated the damage to the specimens.

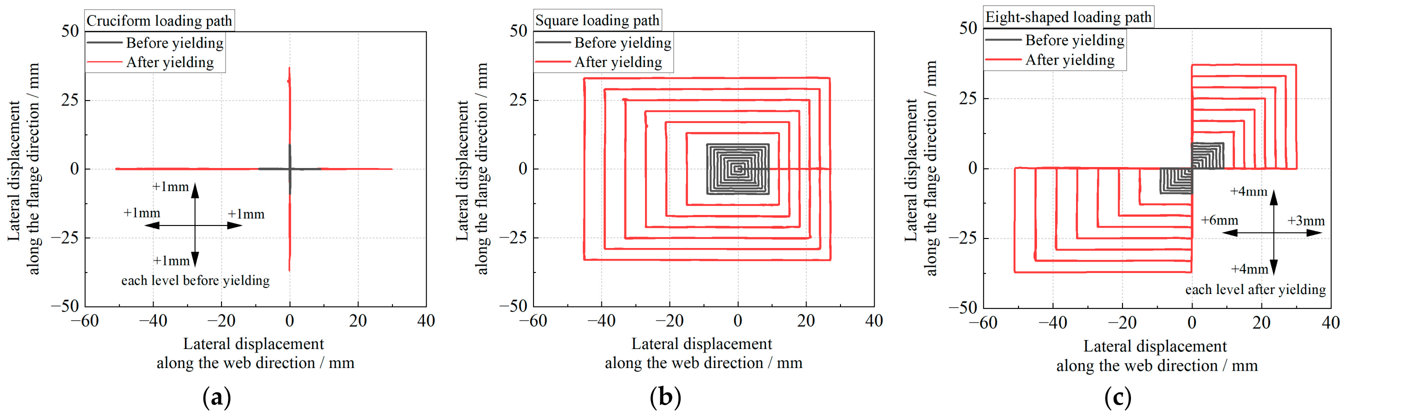

Figure 4. Biaxial displacement applied in the test. (**a**) Cruciform loading path; (**b**) square loading path; (**c**) eight-shaped loading path.

2.2. Numerical Modeling

To thoroughly investigate the seismic performance of slender T-shaped walls under biaxial loading, a numerical model was developed using the open-source computational software OpenSees 3.3.0.

The concrete constitutive model adopted the Concrete02 model [30], which considered the restraint effect of stirrups on concrete and the tensile performance of concrete and has been widely utilized in the numerical studies. The hysteretic constitutive model of Concrete02 is shown in Figure 5a, where concrete in tension is taken as positive. The reinforcement model selected for this study was Steel02, specifically the Giuffre–Menegotto–Pinto model [31]. This model, which is a bilinear model, considers the strain-hardening effect in the same direction as the steel reinforcement and accurately reflects the Bauschinger effect, making it highly similar to the actual steel bar. Figure 5b illustrates the hysteretic relationship of Steel02.

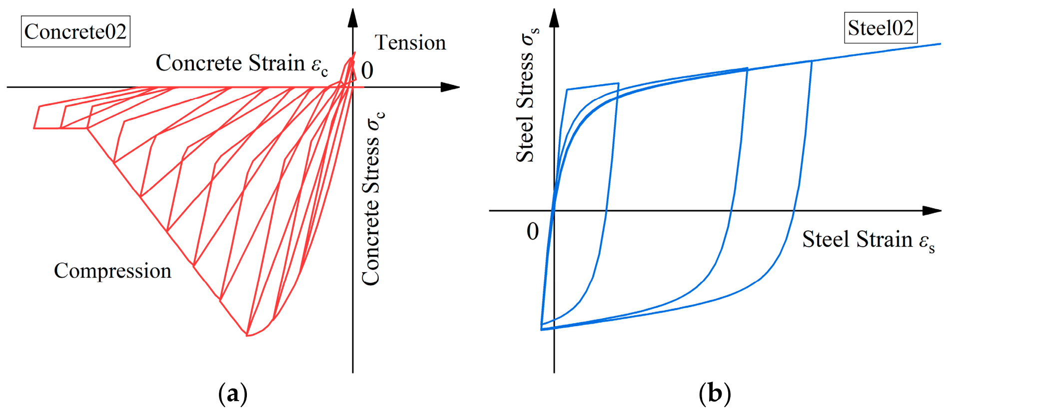

Figure 5. Constitutive relationships in numerical models. (**a**) Hysteretic model of concrete; (**b**) hysteretic model of reinforcement.

The specific parameters of Concrete02 and Steel02 are shown in Tables 1 and 2. The cover concrete and unconfined concrete adopted the same parameters, and the web and flange tips, as well as the web–flange intersection, were taken as the concrete confined by stirrups. When concrete was under compression, the parameters of confined concrete were calculated according to study [30], where $f_{cc} = Kf_{c0}$ and $\varepsilon_c = K\varepsilon_{c0}$. The compressive strength of plain concrete f_{c0} was measured in experiment [19], and the corresponding strain ε_{c0} = 0.002. The concrete crushing strength σ_{cu} was taken as 20% f_{cc}, and the crushing strain $\varepsilon_{cu} = 0.8/Z + \varepsilon_c$. K and Z are determined using the following equations:

$$K = 1 + \rho_{sv} f_{yh} / f_{c0}, \tag{1}$$

$$Z = \frac{0.5}{\frac{3+0.29 f_{c0}}{145 f_{c0} - 1000} + 0.75 \rho_{sv} \sqrt{\frac{h'}{s}} - K\varepsilon_0} \tag{2}$$

In the equations, ρ_{sv} is the volume stirrup ratio, f_{yh} is the yield strength of the stirrup bar, h' is the width of the confined concrete, and s is the spacing of the stirrup. The parameters of tensile concrete were calculated according to the Chinese standard GB 50010 [28], where the tensile softening stiffness E_{ct} was taken as 0.1 times the elastic modulus of concrete E_c.

Table 1. Parameters of Concrete02.

Concrete Type	f_c (MPa)	ε_c	σ_{cu} (MPa)	ε_{cu}	λ [1]	f_t (MPa)	E_{ct} (MPa)
Unconfined concrete	37.63	0.002	7.53	0.0038	0.18	2.3	3200
Flange tip	42.25	0.002246	8.45	0.0181	0.18	2.5	3310
Web–flange intersection area	47.03	0.002499	9.41	0.0331	0.18	2.6	3400
Web tip	48.37	0.002571	9.67	0.0372	0.18	2.7	3430

[1] The parameter λ is the ratio between unloading slope and initial slope, and E_{ct} is the tension softening stiffness.

Table 2. Parameters of Steel02.

Steel Bar	f_y (MPa)	E_s (MPa)	b	R0 [1]	cR1	cR2
Longitudinal bar	469.0	200,000	0.0185	20	0.925	0.15
Vertical distribution bar	448.2	200,000	0.0178	20	0.925	0.15

[1] The parameters R0, cR1, and cR2 are parameters to control the transition from elastic to plastic branches.

The reinforcement included longitudinal bars and a vertical distribution bar. The yield strength f_y and strain-hardening ratio b were determined through the tensile test, the elastic modulus of steel was uniformly taken according to the standard [28], and other parameters were taken as the recommended values [32]. The specific parameters of Concrete02 and Steel02 are shown in Tables 1 and 2.

Fiber sections were chosen as the cross-sectional type for the element in the model. Based on the sectional characteristics, the cross section could be divided into different-sized fiber grids and assigned different constitutive relationships. Taking the web tip as an example, Figure 6 illustrates the division of the fiber section there. Fiber sections can effectively simulate the stress characteristics under an axial force and bending moment, but they cannot express the shear property of the section. Therefore, the Section Aggregator command was used to supplement the shear and torsional stiffness of the section. Table 3 lists the values of stiffness in the fiber section.

The selection of the displacement-based beam–column element (element dispBeam-Column command) was used for the type of element in the model. In order to ensure that the position of the horizontal loading point of the model was consistent with the test, as well as considering the differences in the stress performances of the concrete confinement zone and nonconfined zone due to the large cross section of the specimen, the flange was divided into 5 units and the web was divided into 4 units. The numerical model is shown in Figure 7.

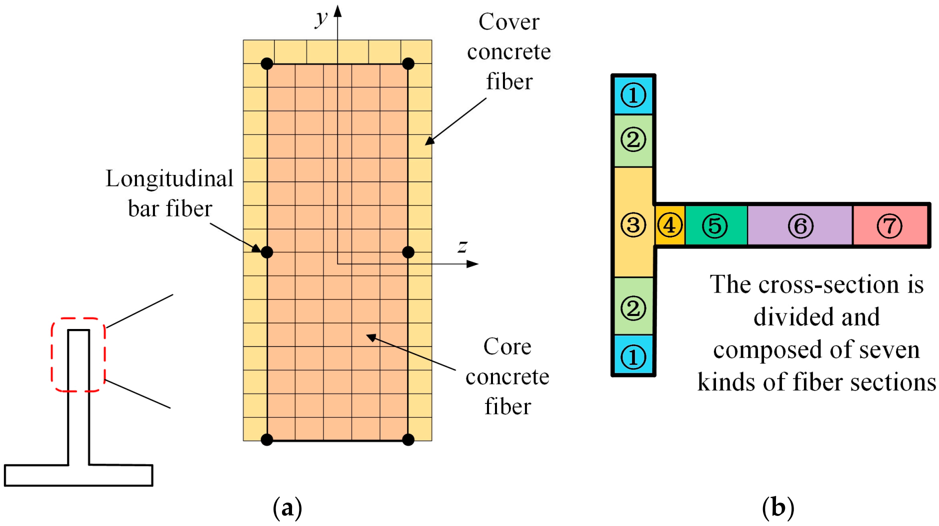

Figure 6. Fiber section of T-shaped wall. (**a**) Fiber meshing of web tip; (**b**) fiber cross-section division.

Table 3. Values of shear and torsional stiffness.

Section Number	Section Region	Shear Stiffness [1]	Torsional Stiffness
1	Flange tip	7.13×10^{8}	1.21×10^{13}
2	Flange unconfined area	1.64×10^{9}	8.68×10^{13}
3	Flange–web intersection 1	1.71×10^{9}	9.73×10^{13}
4	Flange–web intersection 2	4.27×10^{8}	4.90×10^{13}
5	Web unconfined area 1	1.42×10^{9}	6.00×10^{12}
6	Web unconfined area 2	1.99×10^{9}	1.49×10^{14}
7	Web tip	1.85×10^{9}	1.21×10^{14}

[1] The shear stiffness along the section local *y*-axis is equal to that along the local *z*-axis.

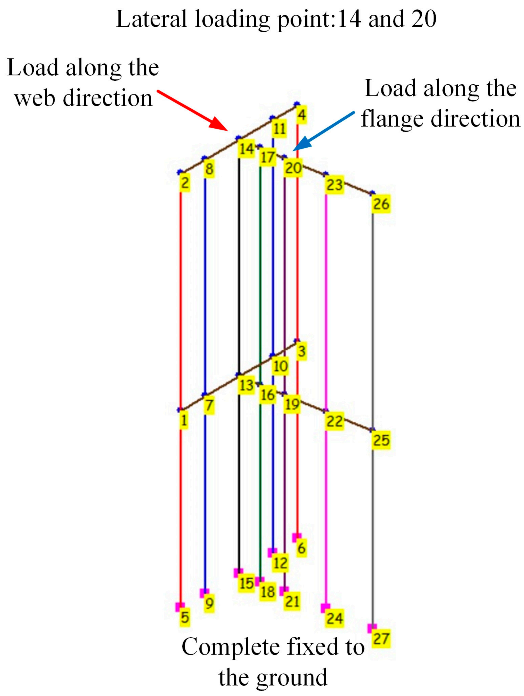

Figure 7. Numerical model of T-shaped wall.

The model adopted the analysis type that axial load was applied first and then horizontal load. First, based on the size of the cross-sectional area of elements, the axial force corresponding to the axial load ratio was proportionally distributed to each element, and the axial force was applied to the top nodes through the Pattern Plain Linear command. Next, the TimeSeries command was used to import two orthogonal displacement files. Various displacement files corresponded to different loading paths, including uniaxial loading along the web and flange directions, cruciform loading path, square loading path, and eight-shaped loading path. Finally, the SP mode of the Pattern Plain command, that is, the single-node-with-multi-degree-of-freedom mode, was used to apply the imported displacements to the web direction of node 14 and the flange direction of node 20 in Figure 7, and it performed horizontal loading according to the same loading protocol as the experiment.

In addition, the six degrees of freedom of all nodes at the bottom of the model were constrained, while no constraints were applied to the top nodes, thereby ensuring that the model had the same boundary conditions as the experiment.

2.3. Model Validation

The established numerical model was used to simulate 5 T-shaped RC shear walls in the experiment [18] to verify the effectiveness of the model. Figure 8 shows the comparison between calculated data and experimental measured load–displacement curves.

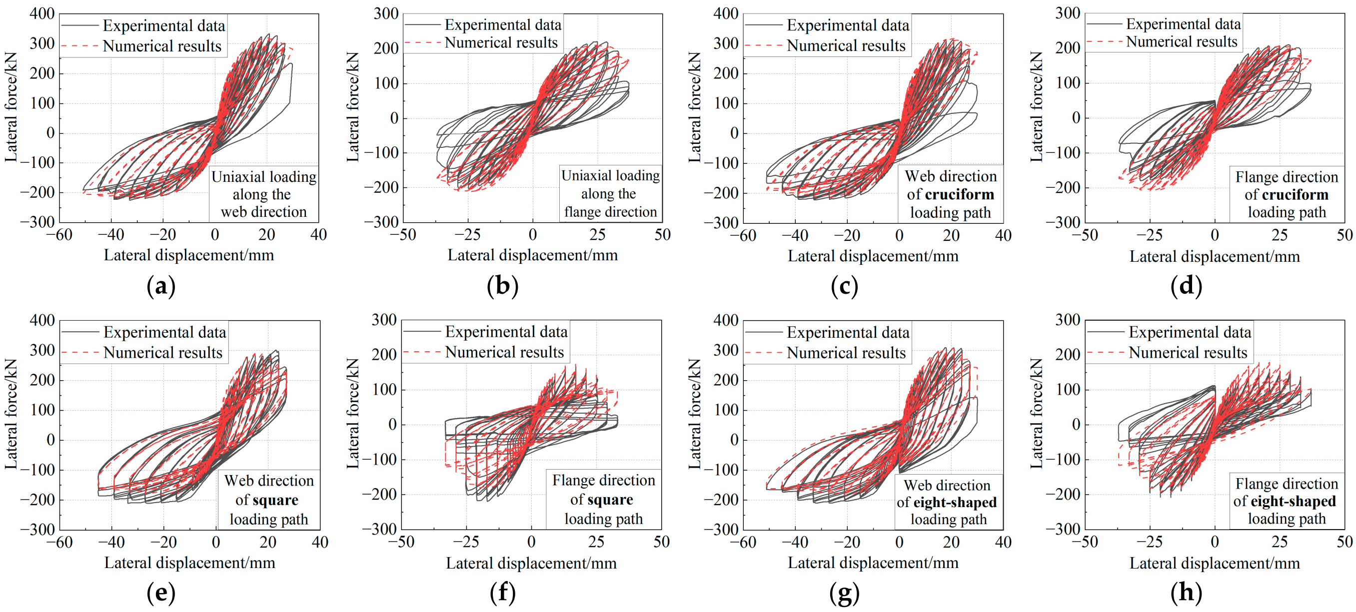

Figure 8. Comparison of hysteresis curves between numerical model and experimental data. (**a**) Uniaxial loading along the web direction; (**b**) uniaxial loading along the flange direction; (**c**) web direction of cruciform loading path; (**d**) flange direction of cruciform loading path; (**e**) web direction of square loading path; (**f**) flange direction of square loading path; (**g**) web direction of eight-shaped loading path; (**h**) flange direction of eight-shaped loading path.

Figure 8 revealed a satisfactory agreement between the hysteresis curves of the model and the experimental curves. The model's curves distinctly exhibited the pinching effect, whereas the shape of the curves remained fundamentally consistent. The curve fit of biaxial loading models was not as good as that of uniaxial loading models, primarily manifested in the certain differences in peak bearing capacity. This was mainly because the role of the stirrups in the model was equivalent to the constraint effect on concrete. Furthermore, the concrete damage was more severe during biaxial loading, which affected the accuracy of the model calculations. The curve accuracy of the cruciform-loaded model was higher than the square- and eight-shaped-loaded models, which was owing to the fact that the T-shaped wall was not in a biaxial coupled stress state under cruciform loading, hence the lesser biaxial coupling effect than that of the two other paths. However, in terms of peak displacement, ultimate displacement, and energy dissipation, the biaxially-loaded model demonstrated higher accuracy. Moreover, the model curves could reflect the characteristics of the vertical variation and intersection of the hysteretic curves caused by biaxial loading. Therefore, the numerical model established in this study was effective.

2.4. Parameter Setting

The chosen parameters were axial load ratio n, shear span ratio λ, flange width to web height ratio b_f/l_w, concrete strength grade, stirrup ratio ρ_v, and longitudinal reinforcement ratio ρ, as listed in Table 4. The axial load ratios selected were 0.1, 0.15, 0.2, 0.25, and 0.3. Simulations were conducted with specimen heights of 1800 mm, 2200 mm, 2600 mm, and 3000 mm, corresponding to shear span ratios of 2.00, 2.44, 2.89, and 3.33, respectively. The flange width to web height ratio varied by changing the flange width to ensure the unity and consistency of the influencing parameters. The flange widths of 580 mm, 740 mm, 900 mm, 1060 mm, and 1220 mm were selected, and the corresponding flange width to web height ratios were 0.64, 0.82, 1.00, 1.18, and 1.36, respectively. According to the specifications on concrete strength in Chinese standard GB 50010 [28], simulations were conducted with concrete strength grades of C30, C35, C40, and C45, and the equivalent compressive strength specified in the American standard were respectively 28.6 MPa, 32.2 MPa, 36.0 MPa, and 39.8 MPa. Study [33] found that the configuration of stirrups at the intersection of the web and flange had little effect on the mechanical performance of T-shaped walls. Therefore, this study only analyzed the influence of the stirrup ratios at the web and flange tips. Stirrup spacings of 175 mm, 125 mm, 75 mm, and 25 mm were selected, and the corresponding stirrup ratios in the web direction were 0.61%, 0.86%, 1.44%, and 4.31%, and in the flange direction, were 0.65%, 0.90%, 1.51%, and 4.52%, respectively. The longitudinal bar diameters of 8 mm, 10 mm, 12 mm, and 14 mm were selected for simulation, and the corresponding longitudinal reinforcement ratios were 0.77%, 1.20%, 1.73%, and 2.35%, respectively.

Table 4. Determined parameters for numerical analysis.

Parameter	Range of Value
Axial load ratio n	**0.10** [1], 0.15, 0.20, 0.25, 0.30
Shear span ratio λ	2.00, **2.44**, 2.89, 3.33
Flange width to web height ratio b_f/l_w	0.64, 0.82, **1.00**, 1.18, 1.36
Concrete strength grade	C30, **C35**, C40, C45
Stirrup ratio ρ_v (%)	0.61, 0.86, **1.44**, 4.31 (web) 0.65, 0.90, **1.51**, 4.52 (flange)
Longitudinal reinforcement ratio ρ (%)	0.77, **1.20**, 1.73, 2.35%

[1] The values in bold represent the parameters used in the standard model.

3. Parametric Study

3.1. Axial Load Ratio

Figure 9 illustrates the envelope curves of the web and flange directions of the slender T-shaped RC walls under different axial load ratios and loading paths. The cumulative energy dissipation of each model, namely the bounding area of the hysteretic curve, is listed in Table 5. The hysteretic curves of each model are not illustrated due to space limitations.

The comparison of the uniaxially- and biaxially-loaded walls revealed that the changes in the bearing capacity, ultimate displacement, and energy dissipation capacity of biaxially-loaded T-shaped walls are consistent with those of uniaxial loading walls. Specifically, as the axial load ratio increased, the bearing capacity in all directions increased, the ultimate displacement decreased, and the total energy dissipation decreased. However, there are significant differences in the values of these three indicators between biaxial loading walls and uniaxial loading.

To further analyze the impact of various parameters on the seismic performance degradation of slender T-shaped RC walls, the decrease ratio of the bearing capacity and ultimate displacement of T-shaped walls was obtained and is plotted in Figure 10. Due to the large amount of data for each model in Figure 10a, it is too lengthy to discuss the impact of the parameters on the biaxial coupling effect for each direction. Therefore, the decrease was analyzed by taking the average value, as shown in Figure 10b. All the decrease ratios were positive, indicating that the biaxial coupling effect weakened the bearing and deformation capacities of T-shaped walls.

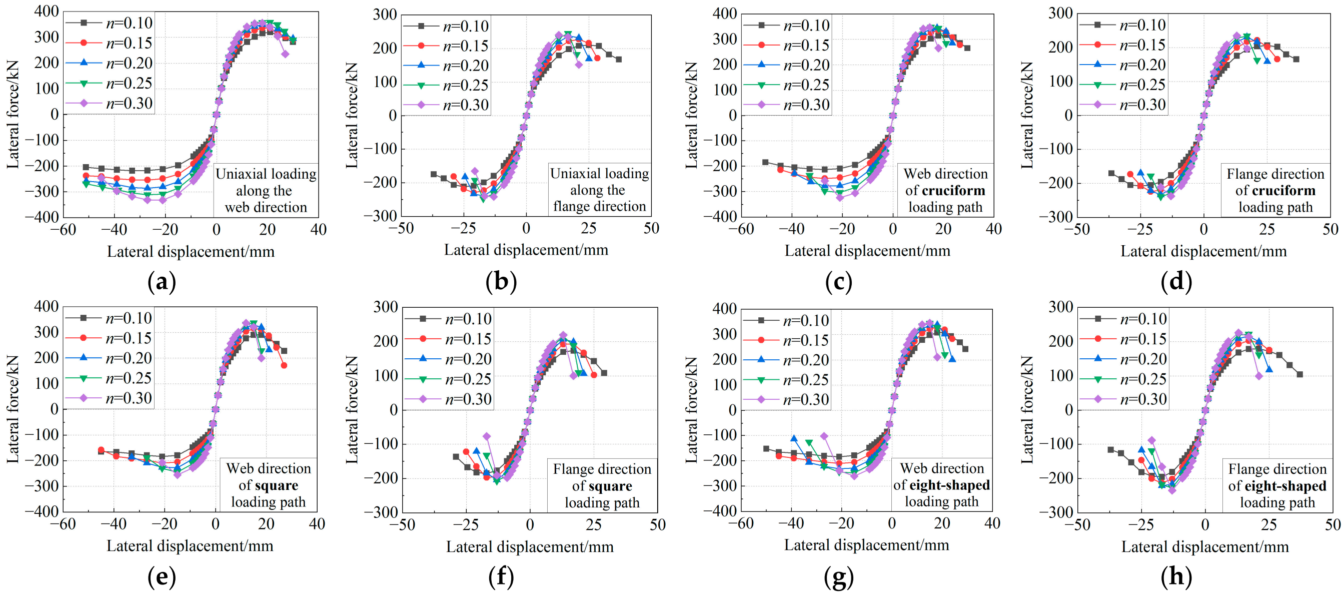

Figure 9. T-shaped wall envelope curves under different axial load ratios. (**a**) Uniaxial loading along the web direction; (**b**) uniaxial loading along the flange direction; (**c**) web direction of cruciform loading path; (**d**) flange direction of cruciform loading path; (**e**) web direction of square loading path; (**f**) flange direction of square loading path; (**g**) web direction of eight-shaped loading path; (**h**) flange direction of eight-shaped loading path.

Table 5. Energy dissipation of T-shaped walls under different axial load ratios (unit: kN·m).

Axial Load Ratio	Energy Dissipation in the Web Direction				Energy Dissipation in the Flange Direction			
	Uniaxial	Cruciform	Square	Eight Shaped	Uniaxial	Cruciform	Square	Eight Shaped
0.10	61.93	59.54	85.93	96.62	41.42	34.68	26.48	25.45
0.15	58.37	56.46	78.30	92.73	25.43	22.41	15.67	10.69
0.20	55.46	43.50	37.85	49.41	19.16	17.88	9.61	6.58
0.25	50.92	29.59	25.63	30.56	13.35	13.69	8.79	6.73
0.30	49.33	21.68	16.74	19.08	11.71	9.76	7.11	6.05

Figure 10b shows that as the axial load ratio increased, the decrease in bearing capacity and ultimate displacement became larger. This was because the increase in the axial load ratio leads to an increase in the compressive strain of the concrete in the compression zone, and the damage of the concrete of the flange and web increased. The biaxial coupling effect further weakened the performance in one direction by the damage in the orthogonal direction, leading to an increase in the decrease in bearing capacity and ultimate displacement.

In terms of energy dissipation, the dissipation in the web and flange directions of the wall under a cruciform path was smaller than that of the uniaxially-loaded wall. This was because the shape of the hysteresis curve under cruciform loading was almost the same as that of the uniaxial loading curve, and the increased damage caused by the biaxial coupling effect reduced the bearing capacity and ultimate displacement, leading to a decrease in the curve surrounding area and energy dissipation.

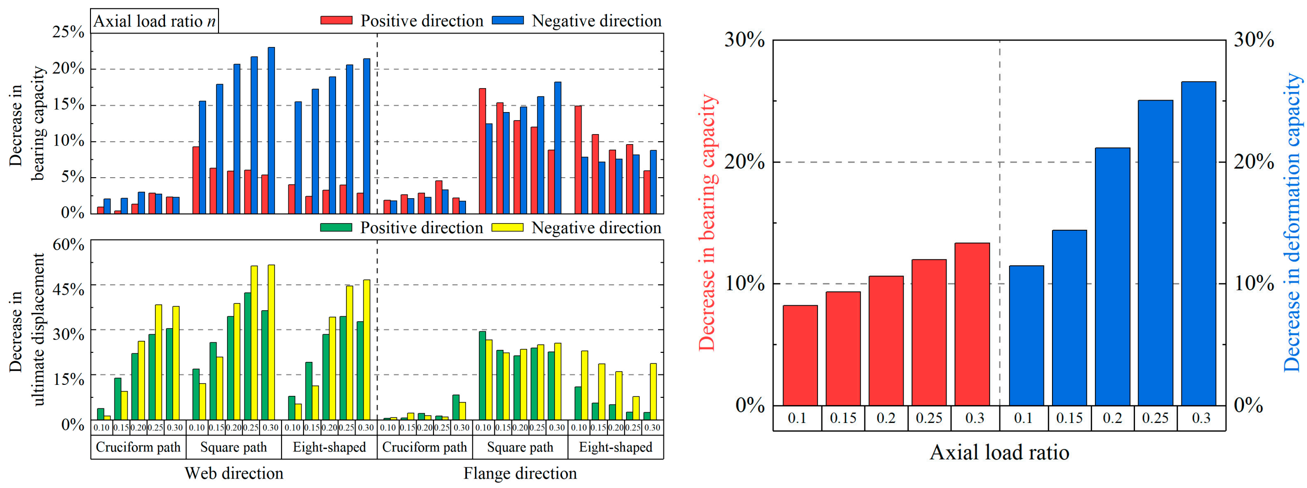

(**a**) (**b**)

Figure 10. Seismic performance degradation under different axial load ratios of T-shaped wall under biaxial loading. (**a**) Degradation in each model; (**b**) average degradation.

The energy dissipation in the web directions of square- and eight-shaped-loaded walls was greater than that of uniaxially-loaded walls when the axial load ratio was small ($n < 0.2$). This was because when the flange direction was loaded, the web direction was in a positive or negative stress state. The simultaneous stress in both directions led to the redistribution of internal forces, indicating that the displacement in the web direction remained unchanged while the force changed. In other words, under these two loading paths, there were vertical variations in the hysteretic curves, leading to an increase in the enveloping area of the curve and an increase in the energy dissipation. The vertical variation segment can be seen from Figure 8e,g. As the axial load ratio continued to increase, the energy dissipation of the two walls was less than that of the uniaxial-loaded wall. This was because the large axial load ratio accelerated the crushing and failure of the concrete in the compression zone, leading to a significant decrease in the deformation capacity and number of hysteretic loops, resulting in a great decrease in the energy dissipation. The energy dissipation in the flange directions of square and eight-shaped loading walls was significantly lower than that of uniaxially-loaded walls. This was also because of the redistribution of internal forces under simultaneous biaxial loading. It resulted in the vertical variation of the curve, leading to the intersection of the unloading curve and loading curve. This can be seen from Figure 8f,h. The intersection of curves significantly reduced the enveloping area of the curve and reduced the energy dissipation. In summary, biaxial loading weakened the energy dissipation capacity of T-shaped walls in a single direction, but the total energy dissipation in both directions of biaxially-loaded walls was greater than that of uniaxially-loaded walls.

3.2. Shear Span Ratio

Figure 11 shows the envelope curves of the web and flange directions of T-shaped walls under different shear span ratios, and Table 6 lists the energy dissipation. The biaxial loading did not alter the variation pattern of performance. As the shear span ratio increased, the bearing capacity in all directions gradually decreased, while the ultimate displacement increased. When the shear span ratio increased to 2.89, the energy dissipation increased significantly. This was because the ultimate displacement increased significantly, leading to a rapid increase in the number of hysteretic loops and a significant increase in the energy dissipation. Similarly, the energy dissipation in the flange direction rapidly increased when the shear span ratio increased to 3.33.

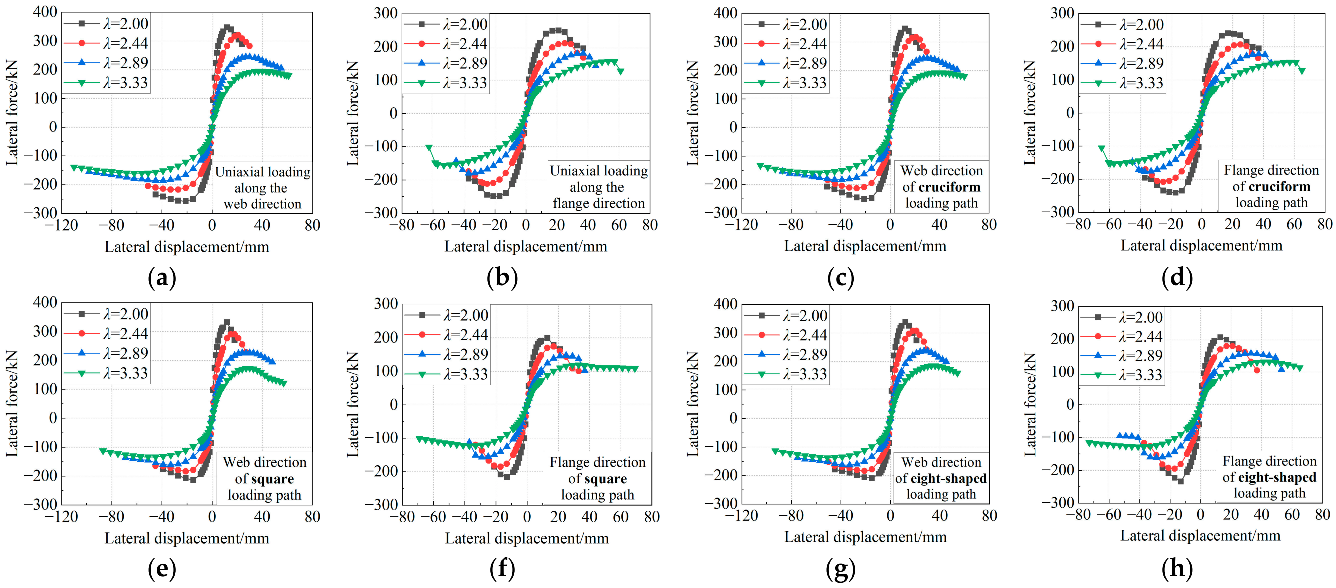

Figure 11. T-shaped wall envelope curves under different shear span ratios. (**a**) Uniaxial loading along the web direction; (**b**) uniaxial loading along the flange direction; (**c**) web direction of cruciform loading path; (**d**) flange direction of cruciform loading path; (**e**) web direction of square loading path; (**f**) flange direction of square loading path; (**g**) web direction of eight-shaped loading path; (**h**) flange direction of eight-shaped loading path.

Table 6. Energy dissipation of T-shaped walls under different shear span ratios (unit: kN·m).

Shear Span Ratio	Energy Dissipation in the Web Direction				Energy Dissipation in the Flange Direction			
	Uniaxial	Cruciform	Square	Eight Shaped	Uniaxial	Cruciform	Square	Eight Shaped
2.00	76.90	72.93	102.93	126.02	45.98	37.35	32.03	27.78
2.44	61.93	59.54	85.93	96.62	41.42	34.68	26.48	25.45
2.89	194.19	171.17	218.01	234.83	35.91	32.47	28.25	17.84
3.33	167.26	150.77	180.66	198.53	49.88	39.87	43.69	40.80

The decrease in the bearing and deformation capacities under different shear span ratios is plotted in Figure 12. As the shear span ratio increased, the decrease in the bearing capacity first reduced and then increased, without a clear pattern, whereas the decrease in the ultimate displacement gradually reduced. This was because the shear-bending coupling of the wall was weakened with the increase in shear span ratio, and the shear strain decreased, leading to a reduction in shear damage. Accordingly, the overall damage of the wall decreased, reducing the biaxial coupling effect, and thus reducing the decrease in ultimate displacement.

The energy dissipation in the web direction under square and eight-shaped loading was always greater than that of uniaxially-loaded walls. This was because under a large shear span ratio, there was no premature crushing and failure of the compressed concrete as in the case of a large axial load ratio, allowing the deformation capacity of the wall to be fully utilized. Therefore, the energy dissipation under these two paths was always greater than that under uniaxial loading.

3.3. Flange Width to Web Height Ratio

Figure 13 illustrates the envelope curves of the web and flange directions of T-shaped walls under different flange width to web height ratios, with Table 7 plotting the energy dissipation of T-shaped walls. When the flange width to web height ratio gradually increased, the bearing capacity in the web direction slightly increased, with a greater increase in the positive direction than the negative direction, whereas the ultimate displacement gradually decreased; at the same time, the bearing capacity in the flange direction increased significantly, whereas the deformation capacity decreased obviously.

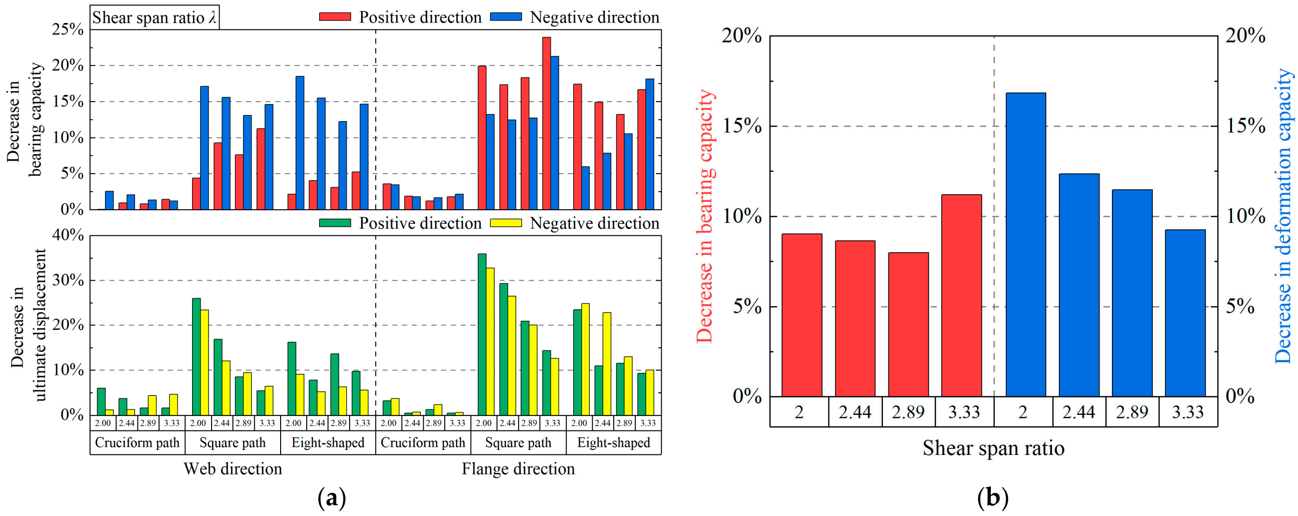

Figure 12. Seismic performance degradation under different shear span ratios of T-shaped wall under biaxial loading. (**a**) Degradation in each model; (**b**) average degradation.

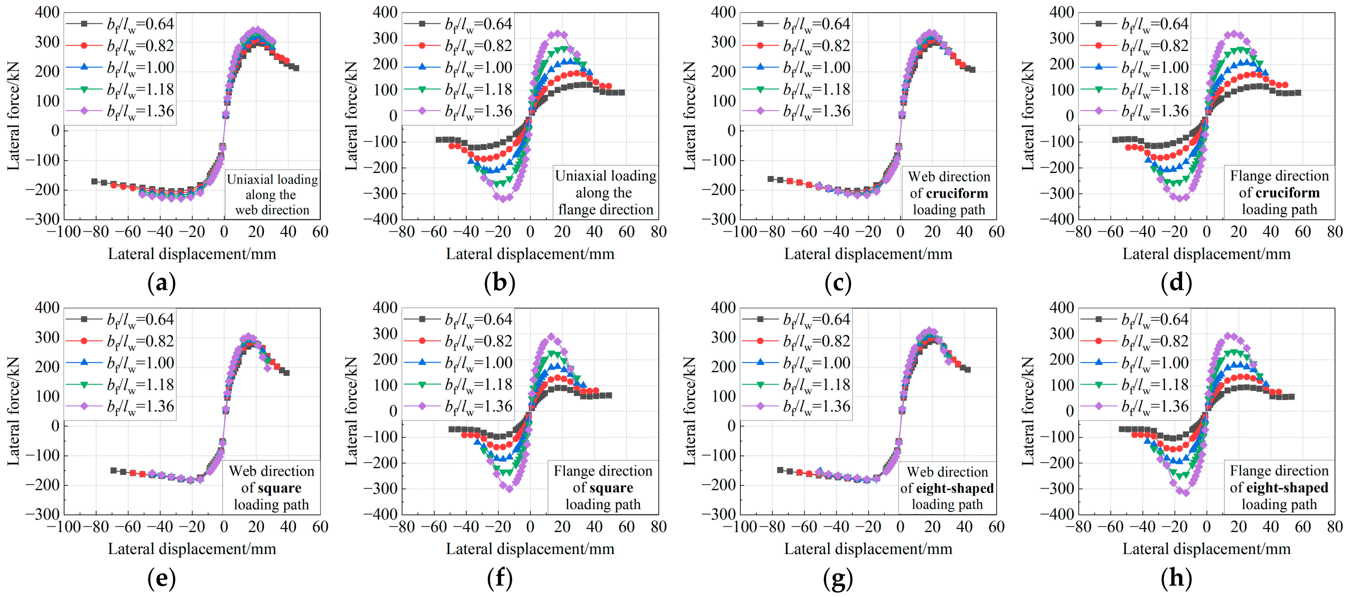

Figure 13. T-shaped wall envelope curves under different flange width to web height ratios. (**a**) Uniaxial loading along the web direction; (**b**) uniaxial loading along the flange direction; (**c**) web direction of cruciform loading path; (**d**) flange direction of cruciform loading path; (**e**) web direction of square loading path; (**f**) flange direction of square loading path; (**g**) web direction of eight-shaped loading path; (**h**) flange direction of eight-shaped loading path.

As the flange width to web height ratio increased, the energy dissipation in the web direction slowly decreased. On the other hand, the energy dissipation in the flange direction increased when the ratio increased from 0.64 to 1.00, and then gradually decreased. This was because in the early stage of the ratio increasing, the ultimate displacement slowly decreased, the total number of hysteretic loops was almost the same, and the total energy consumption increased with the increase in bearing capacity. In the later stage, the ultimate displacement rapidly decreased, and the number of hysteretic loops was greatly reduced, resulting in a decrease in the energy dissipation.

Table 7. Energy dissipation of T-shaped walls under different flange width to web height ratios (unit: kN·m).

Flange Width to Web Height Ratio	Energy Dissipation in the Web Direction				Energy Dissipation in the Flange Direction			
	Uniaxial	Cruciform	Square	Eight Shaped	Uniaxial	Cruciform	Square	Eight Shaped
0.64	79.60	76.16	91.93	99.08	27.80	24.23	17.91	13.63
0.82	73.97	63.51	89.52	98.29	34.94	30.64	23.16	17.88
1.00	61.93	59.54	85.93	96.62	41.42	34.68	26.48	25.45
1.18	58.34	57.86	82.71	92.30	31.48	29.08	22.49	19.92
1.36	56.06	56.57	75.61	90.06	29.87	23.21	21.98	15.72

Due to the change in the flange width to web height ratio by only changing the flange width, the cross-sectional shape of the wall changed, and the decrease in the web and flange directions should not be simply superimposed. Therefore, the average decrease in the bearing capacity and ultimate displacement in both directions is plotted separately in Figure 14b,c. In the web direction, the decrease in bearing capacity increased with the increase in the ratio. This is because increasing the flange width was equivalent to reducing the shear span ratio in the flange direction, and the flange gradually transformed into a squat wall. The loading in the flange direction intensified the damage on the flange, reducing the contribution of the flange to loading in the web direction, thereby increasing the decrease in bearing capacity in the web direction. The ultimate displacement in the web direction was mainly determined by the web tip as the weak stress zone, and the web was located on the symmetrical axis of the flange direction. The loading in the flange direction had little effect on the web tip. Therefore, the ultimate displacement in the web direction changed little. On the other hand, in the flange direction, as the ratio increased, the decrease in the bearing capacity and ultimate displacement gradually reduced. This was because an increase in the flange width increased the bending stiffness of the flange in the web direction, which reduced the damage to the flange caused by loading in the web direction and weakened the biaxial coupling effect. Therefore, the decrease in the bearing capacity and ultimate displacement was reduced.

3.4. Concrete Strength Grade

Figure 15 shows the envelope curves of the web and flange directions of the T-shaped wall under different concrete strengths, and Table 8 lists the energy dissipation under different concrete strengths. With the increase in concrete strength, there was an increase in the bearing capacity and a slight decrease in the ultimate displacement. This was owing to the fact that to maintain a constant axial load ratio, the increase in concrete strength would increase the axial force on the specimen, thus increasing the bearing capacity. Furthermore, the increase in concrete strength also increased the brittleness of the wall, accelerated the crushing of the web and flange tips, and led to a decrease in the deformation capacity. As the concrete strength increased, the energy dissipation in all directions gradually increased. This was because the deformation capacity decreased slightly, the number of hysteretic loops changed little, and the bearing capacity increased, resulting in a gradual increase in the energy dissipation.

Table 8. Energy dissipation of T-shaped walls under different concrete strength grades (unit: kN·m).

Concrete Strength Grade	Energy Dissipation in the Web Direction				Energy Dissipation in the Flange Direction			
	Uniaxial	Cruciform	Square	Eight Shaped	Uniaxial	Cruciform	Square	Eight Shaped
C30	59.69	57.06	83.69	92.40	38.97	32.52	24.71	24.10
C35	61.93	59.54	85.93	96.62	41.42	34.68	26.48	25.45
C40	64.08	61.89	88.69	100.33	43.77	36.79	28.29	26.92
C45	66.09	64.09	91.19	103.87	46.37	38.97	29.67	28.10

The performance degradation of the T-shaped wall under different concrete strength grades is illustrated in Figure 16. As the concrete strength increased, the decrease in the bearing capacity slightly reduced, whereas the decrease in the ultimate displacement increased. This was because the increase in concrete strength led to a decrease in the ultimate compressive strain of the concrete, which made the concrete more susceptible to crushing and increased the brittleness of the wall, aggravating the damage caused by the biaxial coupling effect, and gradually increasing the decrease in ultimate displacement.

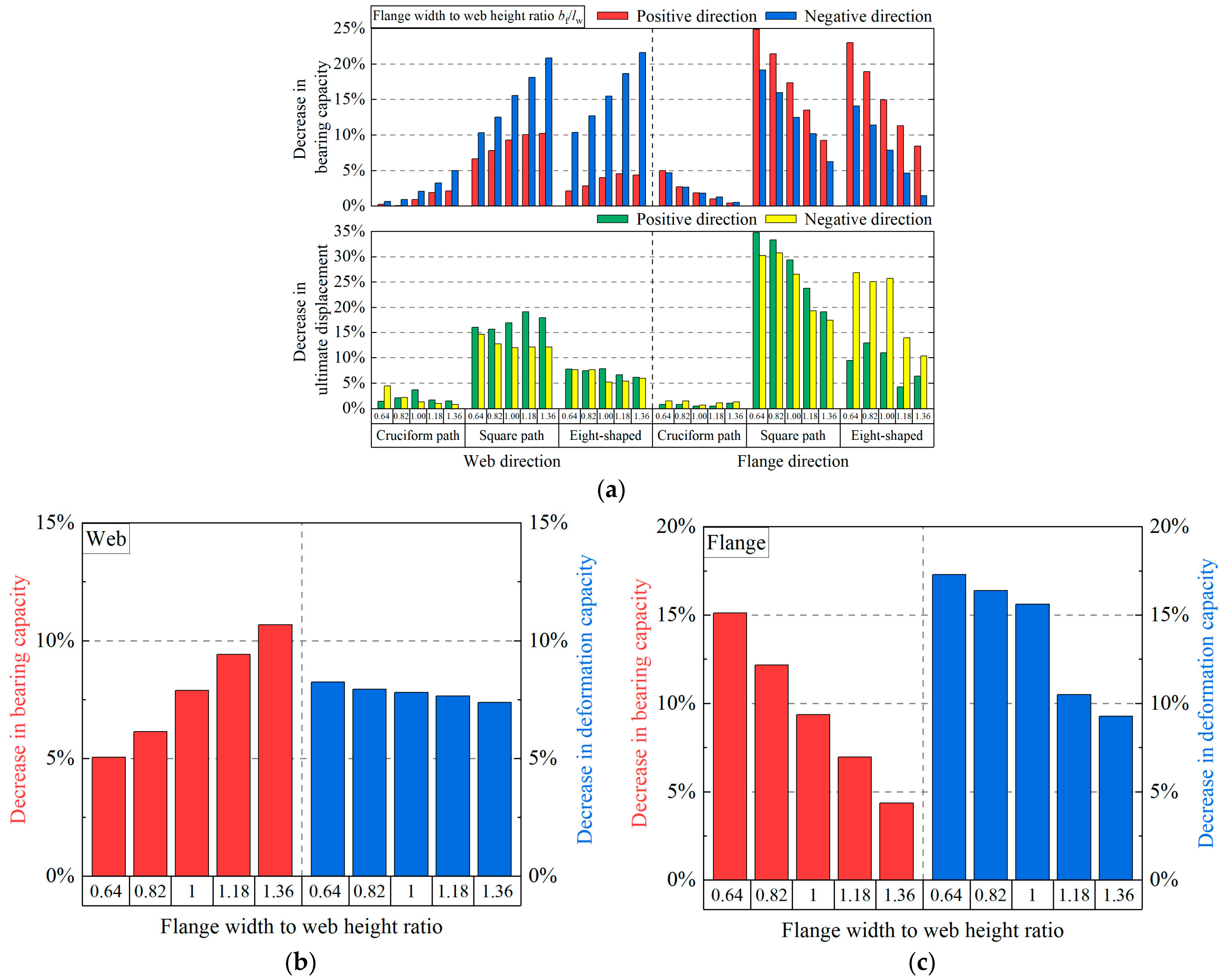

Figure 14. Seismic performance degradation under different flange width to web height ratios of T-shaped wall under biaxial loading. (**a**) Degradation in each model; (**b**) average degradation along the web direction; (**c**) average degradation along the flange direction.

3.5. Stirrup Ratio

Figure 17 shows the envelope curves of the web and flange directions of walls under different stirrup ratios; as well, Table 9 plots the energy dissipation under different stirrup ratios. As the reinforcement ratio increased, the bearing capacity and ultimate displacement of the positive web direction gradually increased. This was because the increase in the stirrup ratio enhanced the compressive strength and ultimate compressive strain of the concrete at the web tip, thereby improving the bearing capacity and deformation capacity in this direction. The performance of the negative web direction remained basically unchanged, because the range of the compression concrete zone in this direction was within the entire flange width, and the increase in the stirrup ratio only improved the mechanical performance of the flange tips, with little impact on the entire flange. In addition, the bearing capacity and ultimate displacement in the flange direction increased with the increase in the stirrup ratio. The energy dissipation also increased with the increase in the stirrup ratio.

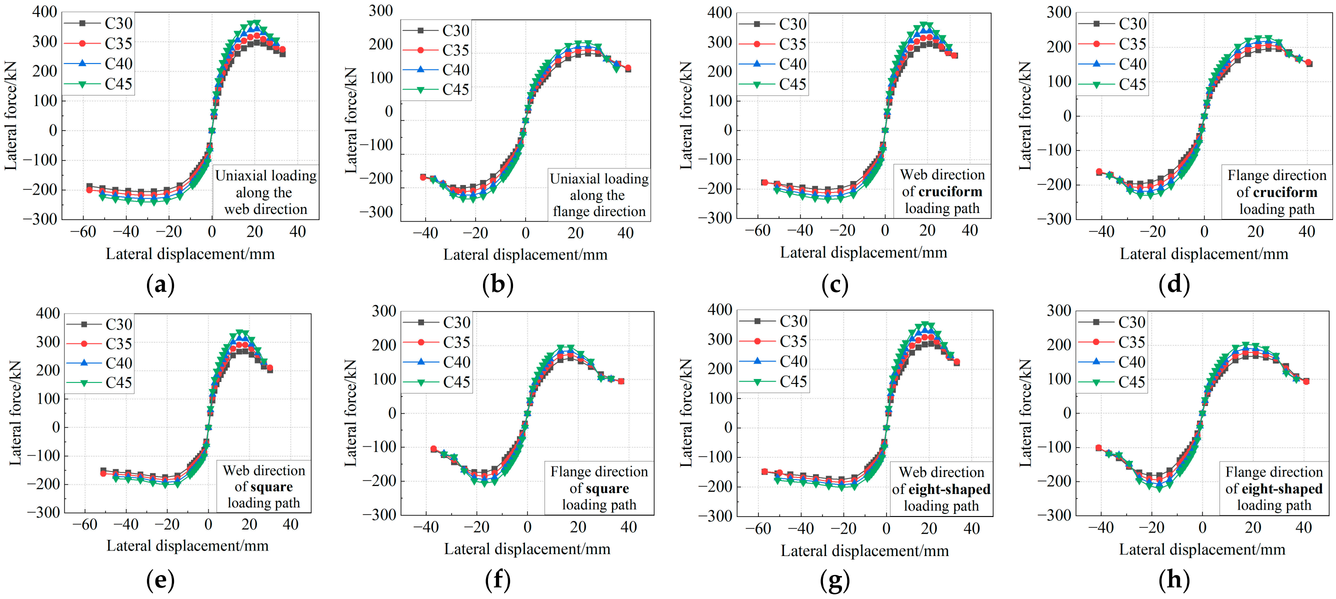

Figure 15. T-shaped wall envelope curves under different concrete strength grades. (**a**) Uniaxial loading along the web direction; (**b**) uniaxial loading along the flange direction; (**c**) web direction of cruciform loading path; (**d**) flange direction of cruciform loading path; (**e**) web direction of square loading path; (**f**) flange direction of square loading path; (**g**) web direction of eight-shaped loading path; (**h**) flange direction of eight-shaped loading path.

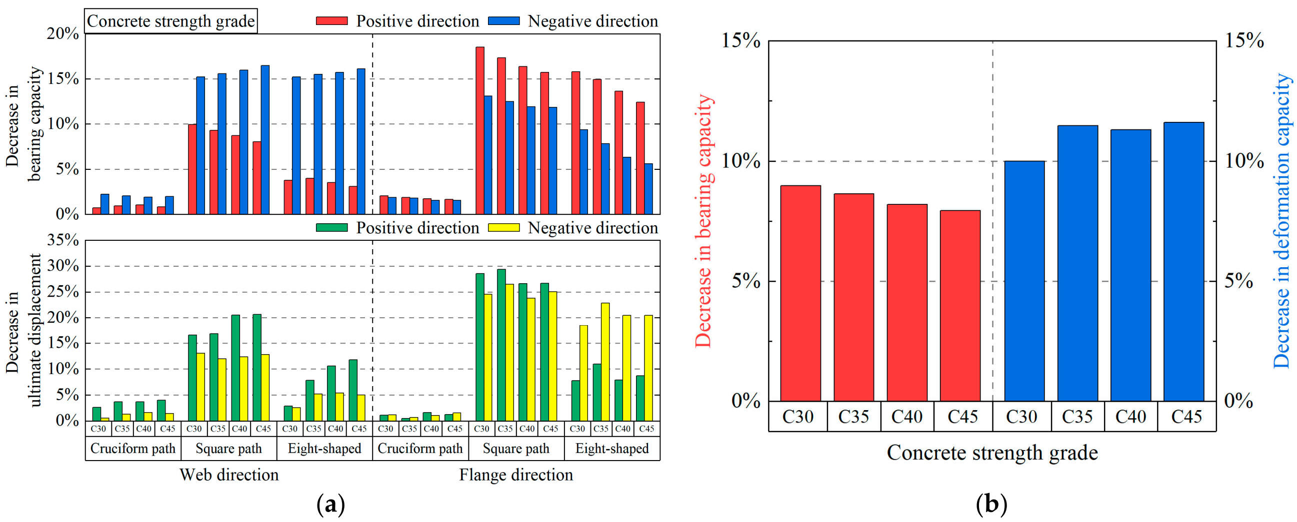

Figure 16. Seismic performance degradation under different concrete strength grades of T-shaped wall under biaxial loading. (**a**) Degradation in each model; (**b**) average degradation.

The decrease in the bearing and deformation capacities under different stirrup ratios is illustrated in Figure 18, where the stirrup ratio is taken as the average value of the web and flange. As the ratio increased, the decrease was almost unchanged, with a variation within 1%. This indicated that the effect of the stirrup ratio on the biaxial coupling effect was very limited.

Table 9. Energy dissipation of T-shaped walls under different stirrup ratios (unit: kN·m).

Stirrup Ratio	Energy Dissipation in the Web Direction				Stirrup Ratio	Energy Dissipation in the Flange Direction			
	Uniaxial	Cruciform	Square	Eight Shaped		Uniaxial	Cruciform	Square	Eight Shaped
0.61%	57.52	56.35	83.27	94.77	0.65%	38.37	30.17	15.30	12.49
0.86%	60.52	58.33	83.7	95.23	0.90%	39.96	31.33	19.30	15.61
1.44%	61.93	59.54	85.93	96.62	1.51%	41.42	34.68	26.48	25.45
4.31%	85.54	82.23	97.38	107.05	4.52%	50.69	43.18	36.44	32.18

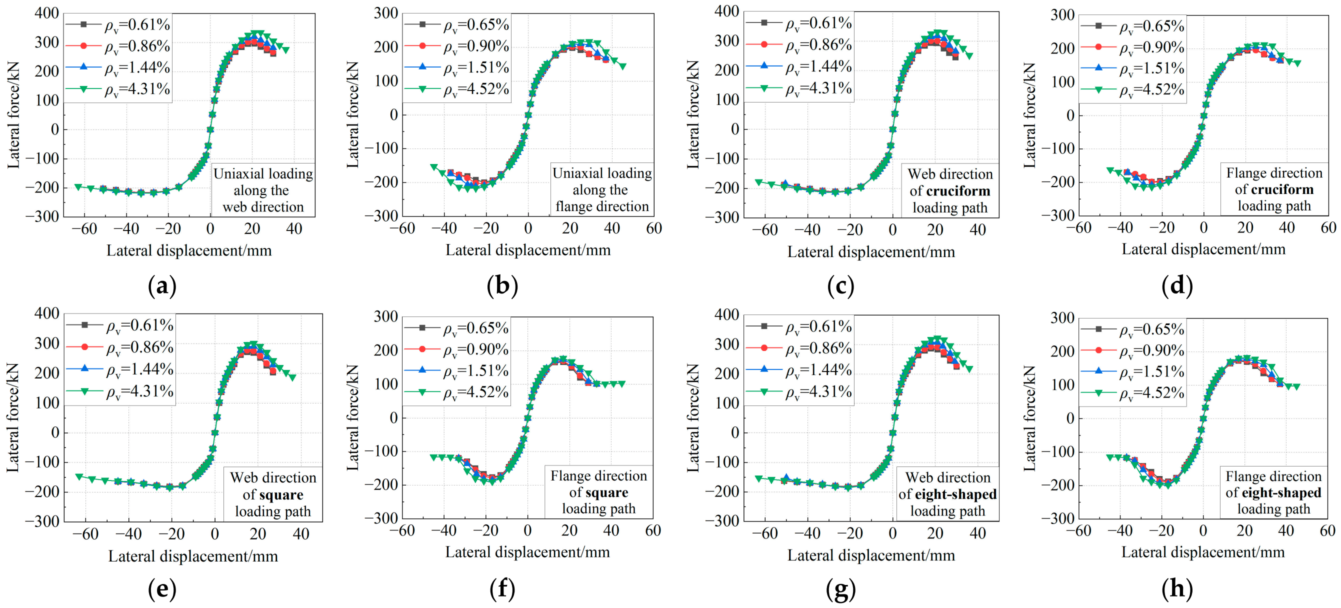

Figure 17. T-shaped wall envelope curves under different stirrup ratios. (**a**) Uniaxial loading along the web direction; (**b**) uniaxial loading along the flange direction; (**c**) web direction of cruciform loading path; (**d**) flange direction of cruciform loading path; (**e**) web direction of square loading path; (**f**) flange direction of square loading path; (**g**) web direction of eight-shaped loading path; (**h**) flange direction of eight-shaped loading path.

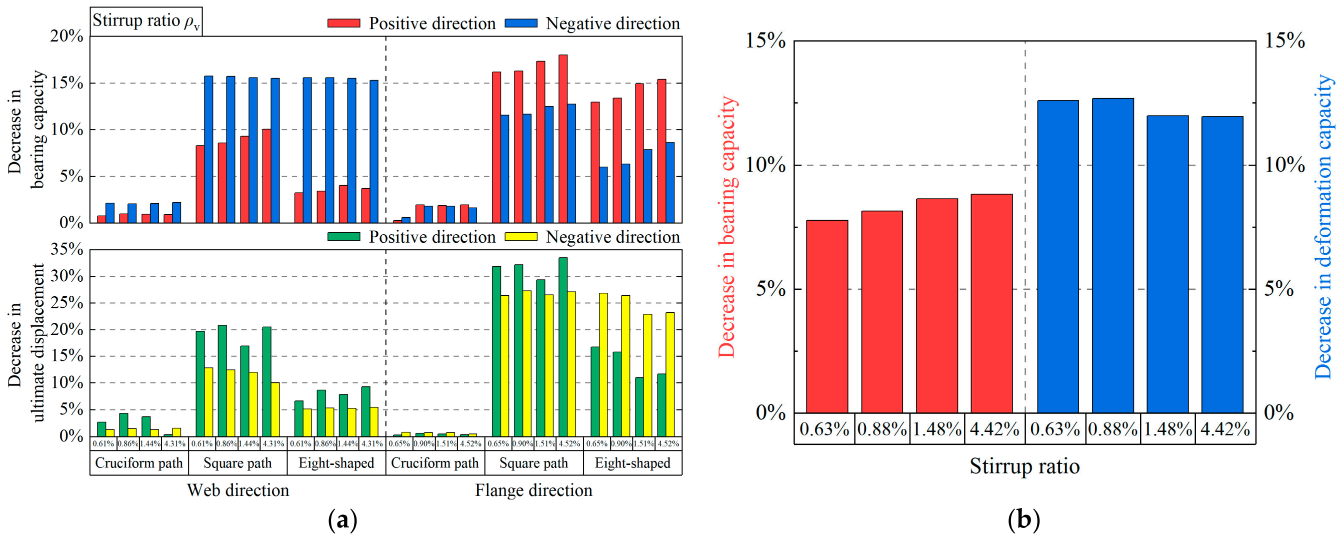

Figure 18. Seismic performance degradation under different stirrup ratios of T-shaped wall under biaxial loading. (**a**) Degradation in each model; (**b**) average degradation.

3.6. Longitudinal Reinforcement Ratio

Figure 19 shows the envelope curves of the T-shaped wall web and flange directions under different longitudinal reinforcement ratios, and Table 10 lists the energy dissipation of T-shaped walls. The bearing capacity in all directions gradually increased, with a more significant increase in the negative web direction than the positive one. On the other hand, the ultimate displacement in all directions slightly decreased, so the energy dissipation in each direction gradually increased with the increase in the longitudinal reinforcement ratio.

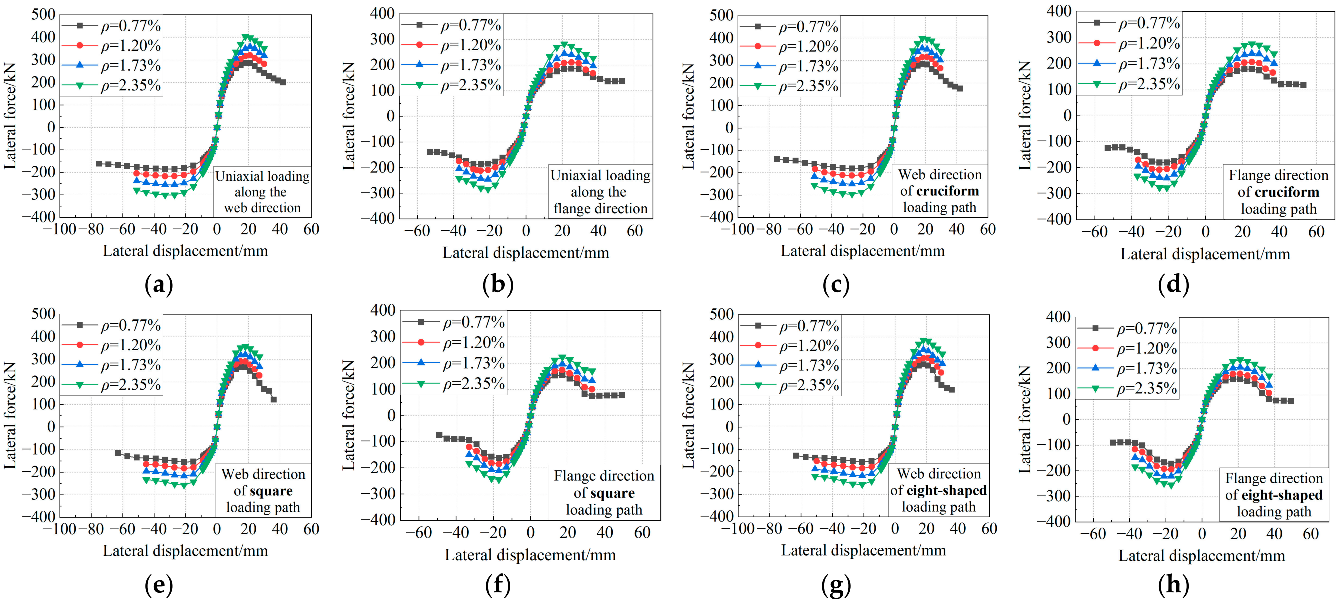

Figure 19. T-shaped wall envelope curves under different longitudinal reinforcement ratios. (**a**) Uniaxial loading along the web direction; (**b**) uniaxial loading along the flange direction; (**c**) web direction of cruciform loading path; (**d**) flange direction of cruciform loading path; (**e**) web direction of square loading path; (**f**) flange direction of square loading path; (**g**) web direction of eight-shaped loading path; (**h**) flange direction of eight-shaped loading path.

Table 10. Energy dissipation of T-shaped walls under different longitudinal reinforcement ratios (unit: kN·m).

Longitudinal Reinforcement Ratio	Energy Dissipation in the Web Direction				Energy Dissipation in the Flange Direction			
	Uniaxial	Cruciform	Square	Eight Shaped	Uniaxial	Cruciform	Square	Eight Shaped
0.77%	51.99	50.74	74.04	85.70	32.01	28.45	21.28	15.32
1.20%	61.93	59.54	85.93	96.62	41.42	34.68	26.48	25.45
1.73%	78.67	75.32	98.43	117.41	57.59	51.61	32.31	33.71
2.35%	97.50	93.11	108.05	131.10	70.66	61.53	38.88	43.10

The performance degradation of T-shaped wall under different longitudinal reinforcement ratios is illustrated in Figure 20. As the ratio increased, there was little fluctuation in the decrease, which was similar to the situation of the stirrup ratio. The biaxial coupling effect was less affected by the longitudinal reinforcement ratio.

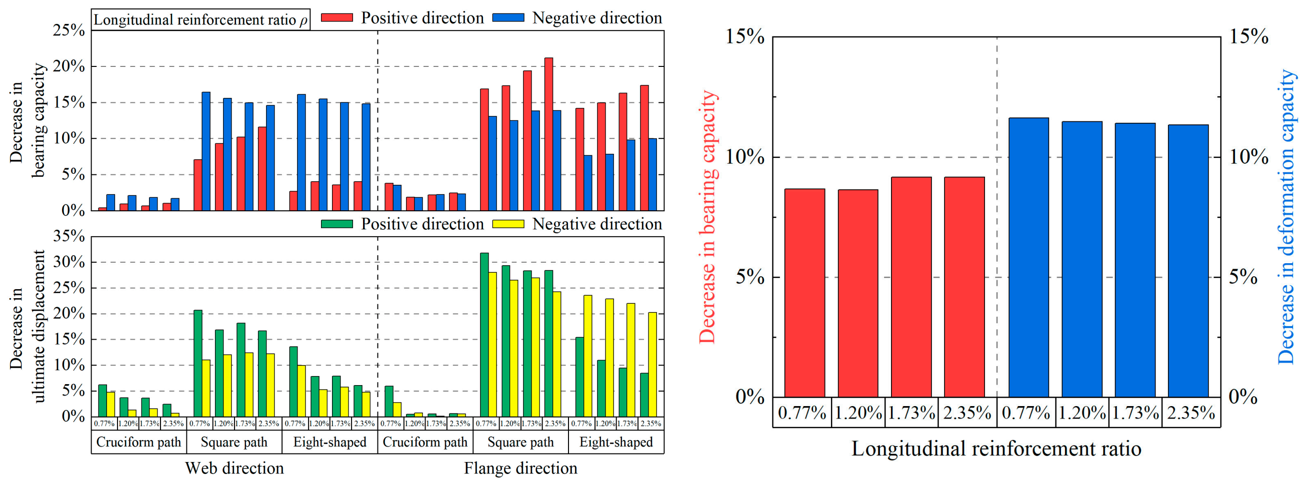

(**a**) (**b**)

Figure 20. Seismic performance degradation under different longitudinal reinforcement ratios of T-shaped wall under biaxial loading. (**a**) Degradation in each model; (**b**) average degradation.

4. Degradation of Seismic Performance under Biaxial Loading

4.1. Influences of Various Parameters

The decrease in the bearing capacity and ultimate displacement of T-shaped walls varied with the change in parameter values. The analysis in the previous section revealed that the changes in some parameters had a relatively small impact on the decrease values, with fluctuations within 1%, whereas changes in other parameters resulted in significant fluctuations in the decrease value. It is worth noting that the variation trends of the decrease values in different directions with the changes in different parameters were also different, making it difficult to find a clear consistent pattern. This was related to the complex mechanism of the biaxial coupling effect as well as the different mechanisms and degrees of impact of different parameters on the mechanical performance of T-shaped walls.

4.2. Comparison of Degradation in Different Directions

For a more intuitive comparison of the decrease in different directions, the average values of decrease in each direction are depicted in Figure 21. In the web direction, the decrease in the bearing capacity in the positive direction was generally smaller than that in the negative direction, which was attributed to the superposition of damage to the flange caused by biaxial loading. Severe damage significantly reduced the contribution of the flange to the bearing capacity during negative loading, leading to an obvious decrease in the bearing capacity. When subjected to positive loading, the web tip was in the compression zone, and the loading in the flange direction had little impact on the damage of the web tip. Therefore, the decrease in the positive bearing capacity of the web under biaxial loading was relatively small.

The decrease in the deformation capacity in the positive direction was generally greater than that in the negative direction in the web direction. This was because the damage caused by biaxial loading increased the brittleness of the wall, leading to a significant decrease in the deformation capacity. On the other hand, during negative loading, the T-shaped wall lost its bearing capacity only when the longitudinal bars at the web tip were fractured. However, a little effect in the biaxial loading on the longitudinal bars at this location resulted in little change in the deformation capacity.

In the flange direction, the decrease in the bearing and deformation capacities of the T-shaped wall under a cruciform loading path was basically the same in the positive and negative directions, due to the symmetrical stress on the flange under cruciform loading.

Under square and eight-shaped loading, the overall decrease in the bearing capacity in the positive flange direction was greater than that in the negative direction. This was because when subjected to positive flange loading, the T-shaped wall was in a state of positive displacement in the web direction, which caused additional axial tension on the flange, equivalent to increasing the reduction in bearing capacity in the flange direction. Similarly, when negative loading along the flange direction, the negative displacement in the web direction caused additional axial compression on the flange, which was equivalent to reducing the decrease in the bearing capacity.

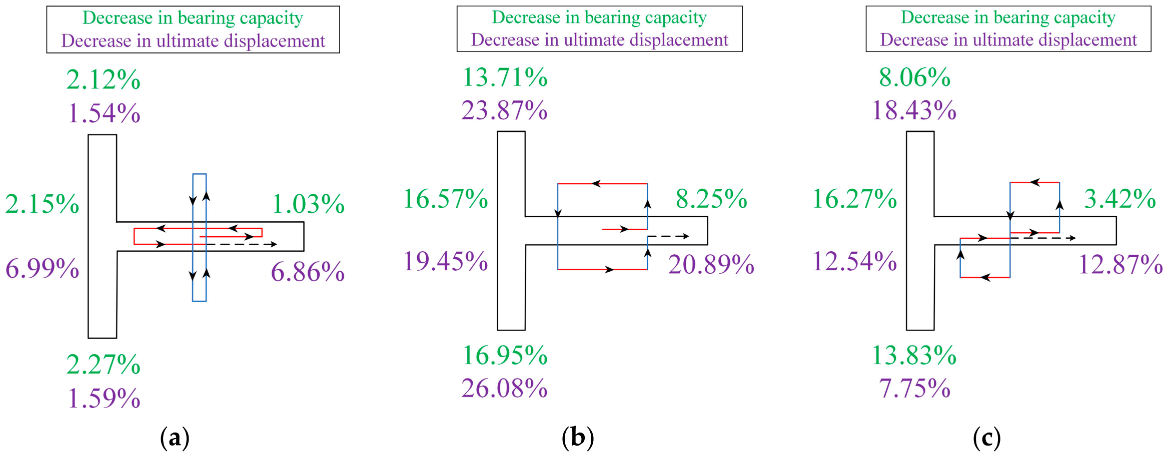

Figure 21. Average decrease in bearing capacity and ultimate displacement under biaxial loading. (**a**) Cruciform loading path; (**b**) square loading path; (**c**) eight-shaped loading path.

In the flange direction, there were differences in the decrease in ultimate displacement between square loading and eight-shaped loading. The walls under square loading exhibited a slightly greater decrease in the positive direction compared to the negative direction, whereas the eight-shaped-loaded walls had a smaller decrease in the positive direction. This could be attributed to the fact that square loading resulted in a relatively equal stress distribution on both sides of the flange, leading to a similar level of damage. However, the positive side of the flange was first damaged in each level of loading, resulting in a slightly greater decrease in the ultimate displacement in the positive direction. On the contrast of eight-shaped loading, the positive side of the flange was not subjected to additional axial compression, leading to less damage and therefore a smaller decrease in the ultimate displacement in the positive direction.

The overall decrease in the web direction and flange direction was compared. Under cruciform loading, the decrease in the bearing capacity in both directions was almost the same, whereas the decrease in the deformation capacity in the web direction was slightly greater than that in the flange direction. This indicated that under cruciform loading, the impact of damage in the two directions on its orthogonal bearing capacity was basically the same, whereas the impact of damage in the flange direction on the deformation capacity in the web direction was greater than that of the web on the flange direction. Under square and eight-shaped loading, the overall decrease in the bearing and deformation capacities in the flange direction was greater than that in the web direction, indicating that the damage in the flange direction was more severe under square and eight-shaped loading than in the web direction.

4.3. Comparison of Degradation under Different Biaxial Loading Paths

A comparison of the decrease of the bearing capacity and ultimate displacement under different biaxial loading paths revealed that the influence of the biaxial loading paths on the decrease values was consistent under different parameter variations. This was manifested by the square loading path causing the greatest decrease in the bearing capacity and ultimate displacement of the T-shaped wall, followed by the eight-shaped path, and the cruciform path causing the lowest decrease. This indicated that the biaxial coupling effect was most severe under the square loading path, resulting in the greatest degradation in the seismic performance of T-shaped walls.

4.4. Sensitivity Analysis of Various Parameters

The above analysis found that the range of changes in the decrease caused by the changes in different parameters varied. Accordingly, a sensitivity analysis was used to study the impact of changes in different parameters on the decrease of bearing and deformation capacities.

The sensitivity coefficient M_a is adopted to quantitatively describe the impact of the changes in parameters on the reduction of the bearing and deformation capacities of T-shaped walls under biaxial loading. M_a is calculated as:

$$M_a = (\Delta S/S)/(\Delta a/a), \tag{3}$$

where Δa is the difference between the parameter value and the reference value a, while ΔS represents the difference between the reduction of the parameter at any value and the reduction S corresponding to the reference value a. In this study, ΔS was taken as the range of decrease in each direction, which was the difference between the maximum and minimum values, while the reference value S represented the minimum value. Δa and a respectively represented the difference and reference value of the corresponding parameter. In addition, the sensitivity coefficient can be positive or negative, so its absolute value was taken for comparison. Figure 22 shows the sensitivity coefficients of various parameters to the reduction in the bearing capacity and ultimate displacement under biaxial loading, with the green curve representing the average values of the two data sets.

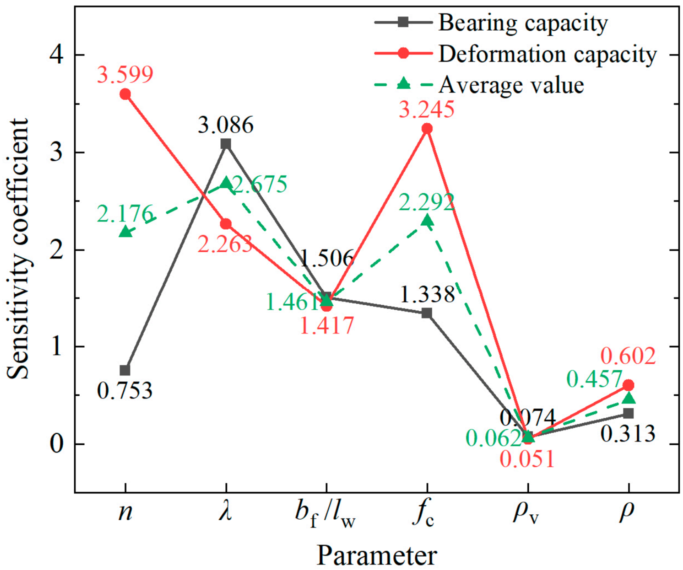

Figure 22. Sensitivity coefficient.

The sensitivity coefficients of each parameter were not the same, and the coefficient values of the same parameter on the reduction in the bearing capacity and deformation capacity were also different. Overall, the sensitivity coefficients of the axial load ratio, shear span ratio, and concrete strength were relatively high, indicating that changes in these three parameters could lead to significant fluctuations in the reduction in bearing and deformation capacities, which significantly affected the performance degradation of T-shaped walls under biaxial loading. Therefore, it is recommended to reasonably consider the values of these three parameters in multidimensional seismic design to maintain safety redundancy.

5. Conclusions

In this study, a numerical model of slender T-shaped RC walls with high accuracy was established. The seismic performance of T-shaped walls under horizontal biaxial loading was parametrically investigated. The decrease in the bearing capacity and ultimate displacement of the biaxial loaded models were computed, and the weakening effect of biaxial loading on the seismic performance of slender T-shaped walls was analyzed. Furthermore, a sensitivity analysis of various parameters for the decrease was conducted. The conclusions are as follows:

(1) Under biaxial loading, the variation trend in the hysteretic behavior of the T-shaped wall was consistent with that of uniaxial loading, and the bearing and deformation capacities decreased. Among the loading paths, the seismic performance of slender T-shaped RC walls was most significantly reduced under a square loading path, followed by an eight-shaped loading path, and the cruciform loading path had the least reduction.

(2) Biaxial loading weakened the energy dissipation capacity in a single direction, but the total energy dissipation in both directions was significantly greater than that of the uniaxially-loaded wall.

(3) Under biaxial loading, the mechanisms of various parameters affecting the biaxial coupling effect were different, resulting in significant differences in the impact of various parameters on the reduction. Different loading paths led to varying degrees of performance degradation, and the seismic performance in the flange direction was more reduced than in the web direction.

(4) Changes in the axial load ratio, shear span ratio, and concrete strength led to significant fluctuations in the reduction in the bearing capacity and deformation capacity, which significantly affected the degradation of the seismic performance of T-shaped walls under biaxial loading. Therefore, it is recommended to reasonably consider the values of these three parameters in a multidimensional seismic design to maintain safety redundancy.

Author Contributions: Conceptualization, M.W. and B.W.; methodology, B.W.; software, M.W.; validation, W.C. and M.W.; formal analysis, W.C.; investigation, M.W.; resources, Q.S.; data curation, M.W.; writing—original draft preparation, M.W.; writing—review and editing, B.W.; visualization, M.W.; supervision, Q.S.; project administration, B.W.; funding acquisition, B.W. All authors have read and agreed to the published version of the manuscript.

Funding: This research was funded by the National Natural Science Foundation of China, grant numbers 52278215 and 51808435.

Data Availability Statement: The data presented in this study are available on request from the corresponding author. The data are not publicly available due to privacy.

Conflicts of Interest: The authors declare no conflicts of interest. The funder had no role in the design of the study; in the collection, analyses, or interpretation of data; in the writing of the manuscript; or in the decision to publish the results.

References

1. Smyrou, E.; Sullivan, T.; Priestley, N.; Calvi, M. Sectional response of T-shaped RC walls. *Bull. Earthq. Eng.* **2013**, *11*, 999–1019. [CrossRef]
2. Ma, K.; Ma, Y.; Liang, X. Seismic behavior of steel reinforced high-strength concrete composite walls. *J. Earthq. Eng.* **2020**, *24*, 1290–1310. [CrossRef]
3. Blount, S.; Ryan, K.; Henry, R.; Lu, Y.; Elwood, K. Evaluation of design modifications for enhanced repairability of reinforced concrete walls. *Eng. Struct.* **2020**, *206*, 110034. [CrossRef]
4. Wei, F.; Chen, H.; Xie, Y. Experimental study on seismic behavior of reinforced concrete shear walls with low shear span ratio. *J. Build. Eng.* **2022**, *45*, 103602. [CrossRef]
5. Dong, Y.; Xu, Z.; Li, Q.; He, Z.; Yan, X.; Cheng, Y. Tests and micro–macro cross-scale model of high-performance acrylate viscoelastic dampers used in structural resistance. *J. Struct. Eng.* **2023**, *149*, 04023088. [CrossRef]
6. Wang, B.; Wu, M.; Shi, Q.; Cai, W. Seismic performance of flanged RC walls under biaxial cyclic loading. *J. Build. Eng.* **2023**, *64*, 105632. [CrossRef]
7. Thomsen, J.; Wallace, J. Displacement-based design of slender reinforced concrete structural walls: Experimental verification. *J. Struct. Eng.* **2004**, *130*, 618–630. [CrossRef]

8. Ji, X.; Liu, D.; Qian, J. Improved design of special boundary elements for T-shaped reinforced concrete walls. *Earthq. Eng. Eng. Vib.* **2017**, *16*, 83–95. [CrossRef]
9. Ke, X.; Qin, Y.; Chen, S.; Li, N. Seismic performance and shear lag effect of T-shaped steel plate reinforced concrete composite shear wall. *Eng. Struct.* **2023**, *289*, 116303. [CrossRef]
10. Ni, X. Hysteretic behavior of T-shaped walls reinforced by high-strength bars: Cyclic loading tests and modelling. *Structures* **2021**, *33*, 1376–1393. [CrossRef]
11. Han, J.; Shu, G.; Qin, Y.; Zhou, G.; Zhou, X. Experimental seismic behavior of T-shaped double skin composite wall with steel truss. *J. Constr. Steel Res.* **2021**, *184*, 106776. [CrossRef]
12. Roy, R.; Acharjya, A.; Roy, A.; Santra, A.; Bhattacharya, G. Response of structures to bidirectional seismic loading: Research progress and future directions. *J. Struct. Eng.* **2022**, *148*, 03122002. [CrossRef]
13. Al-Zuhairi, A.; Al-Ahmed, A.; Hanoon, A.; Abdulhameed, A. Structural Behavior of Reinforced Hybrid Concrete Columns under Biaxial Loading. *Lat. Am. J. Solids Struct.* **2021**, *18*, e390. [CrossRef]
14. Ile, N.; Reynouard, J. Behaviour of U-shaped walls subjected to uniaxial and biaxial cyclic lateral loading. *J. Earthq. Eng.* **2005**, *9*, 67–94. [CrossRef]
15. Kitada, Y.; Nishikawa, T.; Takiguchi, K.; Maekawa, K. Ultimate strength of reinforce concrete shear walls under multi-axes seismic loads. *Nucl. Eng. Des.* **2007**, *237*, 1307–1314. [CrossRef]
16. Beyer, K.; Dazio, A.; Priestley, M. Quasi-static cyclic tests of two U-shaped reinforced concrete walls. *J. Earthq. Eng.* **2008**, *12*, 1023–1053. [CrossRef]
17. Zhang, Z.; Li, B. Seismic performance assessment of slender T-shaped reinforced concrete walls. *J. Earthq. Eng.* **2016**, *20*, 1342–1369. [CrossRef]
18. Brueggen, B.; French, C.; Sritharan, S. T-shaped RC structural walls subjected to multidirectional loading: Test results and design recommendations. *J. Struct. Eng.* **2017**, *143*, 04017040. [CrossRef]
19. Wang, B.; Wu, M.; Shi, Q.; Cai, W. Effects of biaxial loading path on seismic behavior of T-shaped RC walls. *Eng. Struct.* **2022**, *273*, 115080. [CrossRef]
20. Lan, W.; Zhang, Z.; Li, B. Seismic performance of T-shaped steel-concrete composite structural walls subjected to loadings from different directions. *J. Constr. Steel Res.* **2017**, *128*, 7–18. [CrossRef]
21. Ma, J.; Zhang, Z.; Li, B. Experimental Assessment of T-Shaped Reinforced Concrete Squat Walls. *ACI Struct. J.* **2018**, *115*, 621–634. [CrossRef]
22. Eom, T.; Nam, H.; Kang, S. Biaxial interaction and load contour method of reinforced concrete T-shaped structural walls. *ACI Struct. J.* **2018**, *115*, 151–161. [CrossRef]
23. Kolozvari, K.; Gullu, M.; Orakcal, K. Finite element modeling of reinforced concrete walls under uni- and multi-directional loading using Opensees. *J. Earthq. Eng.* **2022**, *26*, 6524–6547. [CrossRef]
24. Ahmed, A.; Mohamed, E. Seismic collapse risk assessment of low-aspect-ratio reinforced concrete shear walls using the FEMA P695 methodology. *J. Struct. Eng.* **2023**, *149*, 04022237. [CrossRef]
25. Waugh, J.D. Nonlinear Analysis of T-Shaped Concrete Walls Subjected to Multi-Directional Displacements. Ph.D. Thesis, Iowa State University, Ames, IA, USA, 2009. [CrossRef]
26. Kolozvari, K.; Kalbasi, K.; Orakcal, K.; Massone, L.; Wallace, J. Shear-flexure-interaction models for planar and flanged reinforced concrete walls. *Bull. Earthq. Eng.* **2019**, *17*, 6391–6417. [CrossRef]
27. Wang, B.; Cai, W.; Shi, Q.; Wu, M.; Li, H. Seismic behavior of RC shear walls with flange based on fiber beam-column element. *J. Build. Struct.* **2021**, *42*, 9. (In Chinese) [CrossRef]
28. *GB 50010-2010*; Code for Design of Concrete Structures. China Architecture and Building Press: Beijing, China, 2010.
29. *JGJ 3-2010*; Technical Specification for Concrete Structures of Tall Building. China Ministry of Housing and Urban-Rural Development: Beijing, China, 2010.
30. Scott, B.; Park, R.; Priestley, M. Stress-strain behavior of concrete confined by overlapping hoops at low and high strain rates. *ACI Struct. J.* **1982**, *79*, 13–27. [CrossRef]
31. Filippou, F.; Popov, E.; Bertero, V. *Effects of Bond Deterioration on Hysteretic Behavior of Reinforced Concrete Joints*; Report EERC 83-19; Earthquake Engineering Research Center, University of California: Berkeley, CA, USA, 1983.
32. Massoni, S.; Mckenna, F.; Fenves, G. *OpenSees Command Language Manual*; Pacific Earthquake Engineering Research (PEER) Center, University of California: Berkeley, CA, USA, 1983.
33. Wang, B.; Shi, Q.; Cai, W. Seismic behavior of flanged reinforced concrete shear walls under cyclic loading. *ACI Struct. J.* **2018**, *115*, 1231–1242. [CrossRef]